

A unified Bayesian approach to kinetic model estimation in dynamic Positron Emission Tomography

Wanchuang Zhu, Jinsong Ouyang, Yothin Rakvongthai, Georges El Fakhri, Yanan Fan *

December 7, 2024

Abstract

We present a fully Bayesian statistical approach to the problem of compartmental modelling in the context of Positron Emission Tomography. We cluster homogeneous region of interest and perform kinetic parameter estimation simultaneously. A mixture modelling approach is adopted, incorporating both spatial and temporal information based on reconstructed dynamic PET image. Our modelling approach is flexible, and provides uncertainty estimates for the estimated kinetic parameters. Crucially, the proposed method allows us to determine the unknown number of clusters, which has a great impact on resulting estimated kinetic parameters. We demonstrate our method on simulated dynamic Myocardial PET data, and show that our method is superior to standard curve-fitting approach.

Keywords: PET, kinetic model, myocardium, spatial mixture model, MCMC

1 Introduction

Dynamic Positron Emission Tomography (PET) can be used to measure tracer kinetics in vivo, from which physiological parameters, such as tissue perfusion, ligand receptor binding potential, metabolic rates, can be determined using compartmental modeling techniques.

Conventional methods for kinetic parameter estimation define a region of interest (ROI) and estimate parameters based on the average. Such methods could be found in Lammertsma and Hume (1996), Slifstein et al. (2008) and Nye et al. (2008). However, conventional methods do not consider spatial heterogeneity. Spatial heterogeneity can be included in voxel-wise estimation methods, which typically perform estimation on the voxel-wise measurement of tracer concentration over time, i.e., the time-activity curve (TAC). Blood samples are usually drawn at appropriate sampling frequency and used as the input to the model. Estimation of the kinetic parameters is typically carried out using a minimum least squares approach (Gunn et al. 1997) or a basis function approach (Gunn et al. 2002). Given low signal-to-noise ratio (SNR), some external constraints are used to stabilize parameter estimation. Smoothness regularization could be found in Kamasak

*W. Zhu and Y. Fan are with School of Mathematics and Statistics, UNSW Australia, Sydney 2052 Australia. J. Ouyang and El Fakhri are with Center for Advanced Medical Imaging Sciences, Massachusetts General Hospital, Boston, MA 02114 and Harvard Medical School, Boston, MA 02115, USA. Y. Rakvongthai is with the Department of Radiology, Faculty of Medicine, Chulalongkorn University, Bangkok 10330, Thailand, the work was performed while the author was with the Center for Advanced Medical Imaging Sciences, Massachusetts General Hospital, Boston, MA 02114, USA and Harvard Medical School, Boston, MA 02115, USA.

et al. (2005) and Huang and Zhou (1998). Also Tikhonov regularization (O'Sullivan and Saha 1999) can be used. Lin et al. (2014) put prior information to stabilize kinetic parameter estimation.

Zhou et al. (2013) provided a Bayesian statistical approach, assuming a Gaussian error distribution. Their approach provided a way of obtaining uncertainty estimates for the kinetic parameters estimated, as well as a model determination tool for the compartmental model. However, all these methods yielded high variance because each voxel was processed independently. This has led to the development of several approaches, in which a clustering method was performed first to cluster the PET images into several homogeneous regions, and kinetic parameter estimations were then performed afterwards based on the averaged values of each cluster. Guo et al. (2003) performed a hierarchical clustering of TACs using a weighted dissimilarity measure. Velamuru et al. (2005) compared a number of different hierarchical clustering algorithms in this context. Mixtures of Gaussians have also been proposed by Ashburner et al. (1996), Aristophanous et al. (2007), Hatt et al. (2009) for static imaging, failing to utilise temporal information. Chen et al. (2001) considered the use of Markov random field (MRF), using a multivariate Gaussian mixture to model the temporal component and the MRF for spatial regularisation. They demonstrated on simulated data a 16 fold decrease in misclassification rate when spatial regularisation was used compared with independent voxel clustering. Kim et al. (2006) presented a method of clustering the TACs using both the temporal and 3D spatial information, where cluster analysis was used first to partition the image based on temporal similarities, and later combined with the 3D spatial information for region growing clustering. Foster et al. (2014) provided a review of clustering methods in PET.

Performing the clustering step separately from kinetic parameter estimation ignores the inherent uncertainties associated with the observed TACs. The bias in the clustering stage is then propagated to the stage of kinetic parameter estimation. Saad et al. (2007) presented a simultaneous clustering and parameter estimation method based on a spatially regularized Kmeans algorithm which iteratively estimated the kinetic parameters in a least squared sense between each cluster update. Mohy-ud Din et al. (2014) proposed a similar algorithm, where the clustering and parameter estimation were performed in an iterative fashion, and they demonstrated the improvements to parameter estimation in myocardial perfusion PET imaging.

We have developed a fully Bayesian approach, which is based on defining a mixture of (unknown number of) multivariate Gaussians to model each voxel-wise TAC. This provides a flexible specification of the error distribution for the TAC. Additionally, we model the spatial dependences between the TACs via the Markov Random Field. The model-based approach offers two advantages as compared to other existing statistical approaches as described above. Given the fact that the true number of mixture components is unknown, our approach determines the optimal number of mixture components and estimates kinetic parameters together with their uncertainties in a single step. We have applied our approach to simulated one-compartment PET perfusion data. We compare the performance of our approach with standard voxel-wise curve-fitting approach using the true kinetic parameters, which are the inputs for the simulation, as the gold standard.

2 Materials and Methods

2.1 Simulated Dynamic Cardiac Perfusion PET Data

All the simulation studies were performed using an NCAT torso phantom (Segars 2000) which consists of heart, lungs, liver, and soft-tissue compartments. The left ventricle (LV) myocardium was segmented into 17 standard segments (Cerqueira et al. 2002). Based on one-tissue compartmental model, TAC, $C_t(t)$, was simulated using:

$$C_t(t) = K_1[C_p(t) \otimes \exp(-k_2t)], \quad (2.1)$$

where $C_p(t)$ is the blood input function, K_1 and k_2 are kinetic rate constants for the segment, and \otimes denotes convolution operation. The kinetic parameters, i.e., $\mathbf{k} = (K_1, k_2)$, assigned to 17 segments were based on the realistic values obtained from PET perfusion studies on normal patients. In order to mimic a myocardial defect, segment located in the anterior wall was assigned with values by lowing K_1 and k_2 by 50% and 20%, respectively, of their original values. We add the 18th segment to include right ventricle (RV) myocardium and other parts. Table 1 shows the kinetic parameters assigned to all the 18 segments in the myocardium. The blood input function $C_p(t)$ and TACs for one normal (basal inferospetal) and one defect (apex) segments are shown in Figure 1.

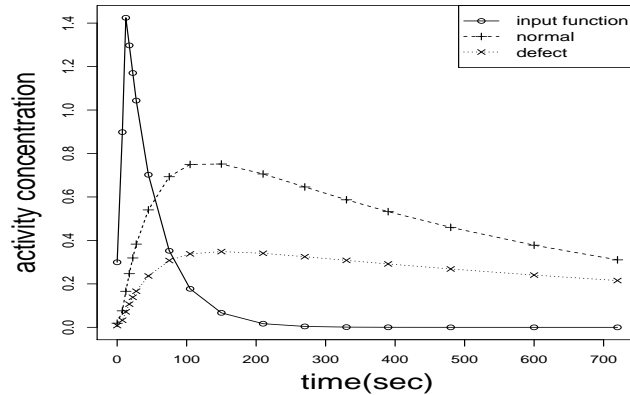


Figure 1: The input function and two TACs (one normal and one defect segment).

segment	K_1	k_2	segment	K_1	k_2
basal anterior	0.3665	0.0627	mid inferior	0.7162	0.0799
basal anteroseptal	0.6730	0.0740	mid inferolateral	0.8013	0.0997
basal inferospetal	0.7656	0.0983	mid anterolateral	0.7720	0.0861
basal inferior	0.7487	0.0635	apical anterior	0.3653	0.0673
basal inferolateral	0.9655	0.1032	apical septal	0.8000	0.0861
basal anterolateral	0.8021	0.0667	apical inferior	0.7544	0.0717
mid anterior	0.3438	0.0541	apical lateral	0.6816	0.1044
mid anteroseptal	0.7799	0.0877	apex	0.3290	0.0554
mid inferoseptal	0.9016	0.0730	others	0.7630	0.0820

Table 1: Segment names and their assigned K_1 , k_2 values (i.e., the ground truth).

The simulated sinogram data is equivalent to a 13-min dynamic PET scan with the framing scheme of $6 \times 5s$, $3 \times 30s$, $5 \times 60s$, and $3 \times 120s$ frames. Twenty five dynamic PET noise realizations were generated. Both attenuation and normalization were included in the simulations, while random and scatter events were not. For each noise realization, the image reconstruction at each time frame was performed using standard ordered subset expectation maximization (OSEM, Hudson and Larkin (1994)) with 16 subsets and 8 iterations.

We obtain the mask of the heart region by blurring the exact mask (used to simulate data) of the myocardium voxels. This mask will hence be bigger than the exact myocardium area. Therefore, noise component is necessary to model the voxels which do not belong to myocardium, but are included in ROI.

2.2 Kinetic Parameter Estimation Using Curve Fitting

Kinetic analysis is performed by curve-fitting the TAC in each voxel using a non-linear least-square fitting:

$$\mathbf{k}_i = \operatorname{argmin} \sum_{t=1}^T w^t (y_i^t - x_i^t(\mathbf{k}_i))^2, \quad (2.2)$$

where y_i^t is the reconstructed activity concentration for voxel i and time frame t , $x_i^t(\mathbf{k}_i) = \frac{1}{\Delta t} \int C_i^t(s; \mathbf{k}_i) ds$, is the average concentration over time frame t , w^t is the weighting factor which herein is chosen to be the squared frame duration divided by the total counts in that frame (Gunn et al. 1997). This nonlinear least square problem can be solved using the Levenberg-Marquardt algorithm (Wang and Qi 2009). We denote this standard curve-fitting approach SCF in this paper.

2.3 A Bayesian Spatial Mixture Model

2.3.1 Model

Here we describe our proposed modelling and estimation approach. Denote the reconstructed activity concentration data by $y_i = (y_i^1, \dots, y_i^T) \in \mathbb{R}^T$ for voxel i . Each data point y_i^t corresponds to the reconstructed activity concentration at time t . We assume that the data y_i can be grouped into G spatially homogenous groups, where within each group, all voxels share the same kinetic rate parameters (or TACs) and their variations are only due to noise (measurement error). The number of groups, G , and the group membership, is treated as unknown and estimated by our approach.

We use a mixture of Multivariate Gaussian with G components to model the noisy data. This allows for a flexible specification of the noise distribution given the fact that the noise distribution in the TAC data is unknown. The Potts model (Wu 1982) is used to account for spatial correlation between the TACs. This is achieved by introducing a set of auxiliary random variables $\mathbf{z} = (z_1, \dots, z_n)$, where z_i takes one of the values $1, \dots, G$, and represents the group/cluster membership for each voxel. Mathematically, each noisy TAC is given by the mixture of T -dimensional Gaussian

$$f(y_i | \boldsymbol{\mu}, \boldsymbol{\Sigma}, \beta) = \sum_{g=1}^G f(z_i = g | \beta) MVN(y_i | z_i = g, \boldsymbol{\mu}_g, \boldsymbol{\Sigma}),$$

where $f(z_i = g | \beta)$ is the density of the Potts model, $MVN(y_i | z_i = g, \boldsymbol{\mu}_g, \boldsymbol{\Sigma})$ is the density of the Multivariate Gaussian, and β is the parameter that reflects the spatial strength between voxels. A value of 0 indicates independence between voxels, while larger values of

β will tend to cluster all voxels into one cluster. The mean vector of the g th Multivariate Gaussian component is denoted by $\boldsymbol{\mu}_g$, and $\boldsymbol{\Sigma} = \text{diag}(\sigma^{2,1}, \dots, \sigma^{2,T})$ is the covariance matrix, assumed to be the same for all mixture components. Here $\sigma^{2,t}, t = 1, \dots, T$ denotes the variance at time t , and the data is assumed to be temporally independent. The mixture model representation allows the error distribution to be more flexible. We refer to our model as the spatial mixture model (SMM).

Within the G components, we allow one component to be the noise component, g^* , that contains only noise and cannot be appropriately modeled by the kinetic equation. We set the mean vector Multivariate Gaussian for g^* as

$$\boldsymbol{\mu}_{g^*} = (\mu_{g^*}^1, \dots, \mu_{g^*}^T),$$

where the $\mu_{g^*}^t, t = 1, \dots, T$ are unknown parameters. For the remaining components $g = 1, \dots, G - 1$, we model the mean vector as a function of the solution to the ordinary differential equation (ODE) describing the one-compartment model (Morris et al. 2004), although extensions to more compartments is straightforward. Hence for $t = 1, \dots, T$, we set

$$\mu_g^t = K_1^g \sum_{\tau=1}^t \hat{C}_p(\tau) \exp(-k_2^g(t - \tau)), \quad (2.3)$$

where $\hat{C}_p(\tau)$ is a measured blood input function. The parameters K_1^g and k_2^g are the kinetic rate parameters specific for group g .

2.3.2 Prior Specifications

For Bayesian inference, we need to specify prior distributions for the unknown parameters $K_1^g, k_2^g, \mu_{g^*}^1, \dots, \mu_{g^*}^T, \sigma^{2,1}, \dots, \sigma^{2,T}, \beta, g = 1, \dots, G - 1$. We assume independent and uninformative priors between all the parameters, such that the priors have a minimal effect on the resulting inference.

For the kinetic rate parameters, we use the Uniform distribution for all g , $K_{1g} \sim \mathcal{U}[a_{K_1}, b_{K_1}]$ and $k_{2g} \sim \mathcal{U}[a_{k_2}, b_{k_2}]$, where \mathcal{U} denotes Uniform distribution. We have used $(a_{K_1}, b_{K_1}) = (0, 1)$ and $(a_{k_2}, b_{k_2}) = (0.03, 0.3)$ in our application. Since we know that K_1 can only take values between 0 and 1, and k_2 is typically small. For the mean vector of the noise component $\mu_{g^*}^t \sim \mathcal{U}[0, \infty)$, for all $t = 1, \dots, T$. We set our prior on β to be $\beta \sim \mathcal{U}[0, b_\beta]$, where we take b_β to be 1, so as to include most of the plausible values of β . Finally, for the variance parameters $\sigma^{2,t}, t = 1, \dots, T$, we take the usual vague conjugate prior with Inverse Gamma distribution $\sigma^{2,t} \sim IG(a, b)$, where $a = 3, b = 10$ for an uninformative prior on $\sigma^{2,t}$.

2.3.3 Markov chain Monte Carlo

Bayesian inference proceeds via the posterior distribution, obtained by the simple product of the likelihood and the priors in Section 2.3.2. The likelihood function is given by

$$f(\mathbf{y}, \mathbf{z} | \boldsymbol{\mu}, \boldsymbol{\Sigma}, \beta) = \prod_{i=1}^n f(y_i | z_i = g, \boldsymbol{\mu}_g, \boldsymbol{\Sigma}) f(\mathbf{z} | \beta). \quad (2.4)$$

Markov chain Monte Carlo algorithms were developed to sample from the posterior distribution, using a combination of Random-Walk Metropolis-Hastings and Gibbs updates. Details for the implementation of the algorithm is given in Appendix. Note that occasionally the identifiability issue arises in the MCMC estimation of mixtures. This can be handled by imposing certain ordering constraints on parameters (Fernández and Green 2002), or via postprocessing of the MCMC output (Frühwirth-Schnatter 2011).

2.3.4 Implementation

We run 6000 MCMC iterations. The speed of convergence was fast, so we keep the final 3000 iterations for inference. We use the proposal distributions $K_1^g \sim N(K_1^g, 0.01^2)$, $k_2^g \sim N(k_2^g, 0.005^2)$, $\mu_{g^*}^t \sim N(\mu_{g^*}^t, 0.001^2)$ and $\beta' \sim N(\beta, 0.005^2)$.

2.3.5 Determination of the Number of Components G

One of the uncertainty of the above model is the selection of the value of G , which plays a crucial role in the resulting parameter estimation. For model-based inference, in which a likelihood is readily available, a number of model selection criteria are available, including Bayesian information criterion (BIC), integrated completed likelihood (ICL), deviance information criterion (DIC) and Akaike information criterion (AIC). The BIC is often considered to be more robust and is the frequently adopted measure of goodness of fit of the model (Steele and Raftery 2009). Our approach uses BIC as the criterion to determine the optimal value of G .

BIC (Schwarz et al. 1978), is given as

$$BIC = -f(\mathbf{y}|G, \hat{\mathbf{z}}_{MAP}, \hat{\theta}) + DF \times (\ln(n) + \ln(2\pi)), \quad (2.5)$$

where $f(\mathbf{y}|G, \hat{\mathbf{z}}_{MAP}, \hat{\theta})$ is the likelihood function corresponding to the model with G components, evaluated at the Maximum a posteriori (MAP) estimator of \mathbf{z} and the posterior means of all the parameters in the corresponding model, $\hat{\theta}$, DF is the number of parameters to be estimated, and n is the number of observations or voxels. BIC penalises models with too many parameters against the maximised log-likelihood (or fit to the data). Optimal choice of G corresponds to the model with the smallest BIC value.

2.3.6 Classification

In our simulated data, voxels with normal tissues have K_1 values ranging from 0.6 to 1, and defect tissues have K_1 values ranging from 0.3 to 0.6. Detailed information for K_1 value and k_2 value can be found in Table 1. In the SMM model, we use the MAP estimator to give voxel-wise classification. For those model, where the number of clusters is not 3, we merge the clusters based on the above rule.

For comparison, we use the K_1 estimation from SCF, and group them according to their K_1 values and we also use the Kmeans method and preset the number of clusters to be 3. Kmeans is implemented to TAC data and membership is obtained.

2.4 Performance Evaluation

For a given noise realization, n , we use computed kinetic parameter bias of voxel i using:

$$b_i^n = (\mathbf{k}_i^n - \mathbf{k}_i^{Tr}) / (\mathbf{k}_i^{Tr}) \quad (2.6)$$

where b_i^n is the bias of estimated kinetic parameter using the true kinetic parameter \mathbf{k}_i^{Tr} as gold standard. Based on 25 noise realizations, we compute the mean \bar{b}_i and standard deviation s_i bias for voxel i using:

$$\bar{b}_i = \frac{\sum_{n=1}^N b_i^n}{N}, \quad s_i = \sqrt{\frac{\sum_{n=1}^N (b_i^n - \bar{b}_i)^2}{N - 1}} \quad (2.7)$$

where N is the total number of noise realizations. We perform the calculations described above for both SCF and SMM methods and make a comparison between the two methods.

3 Results

3.1 Model selection

We implement mixture model for four times with $G = 2$, $G = 3$, $G = 4$ and $G = 5$ respectively. Table 2 shows the BIC values for the four competing models. We can see that the model with only two components does not perform well, because two-component model groups normal and defect tissues in one cluster. In contrast, the model with 3 to 5 components have similar performance in terms of BIC values. The model with $G = 4$ generates the smallest BIC values and was chosen as the optimal model under the BIC. Subsequent results in this paper are generated by the model with $G = 4$.

	$G = 2$	$G = 3$	$G = 4$	$G = 5$
BIC ($\times 10^4$)	-4.7961	-5.3415	-5.4288	-5.3533

Table 2: BIC values for different mixture specifications $G = 2, 3, 4$ and 5 .

3.2 Estimation of Kinetic Parameters using SMM

The mixture model with $G = 4$ components represents the model with three components with kinetic activity and one noise component. Table 3 presents the posterior mean and 95% posterior credibility intervals of the kinetic parameters, i.e., K_1^g and k_2^g , for the three of the four components (the fourth component is noise component where no kinetic activity happens). Figure 2 shows the corresponding posterior distributions of K_1 and k_2 . These results show that the voxels can be clustered into three distinct groups for non-noise components. The first group with $K_1 = 0.3275$ corresponds to defect tissues. The other two groups correspond to normal tissues. Clustering standard can be found in Section 2.3.6.

	K_1^1	K_1^2	K_1^3	k_2^1	k_2^2	k_2^3
mean	0.3275	0.6097	0.7834	0.0520	0.0723	0.0818
2.5% quantile	0.3212	0.6039	0.7765	0.0488	0.0707	0.0803
97.5% quantile	0.3331	0.6149	0.7907	0.0548	0.0736	0.0834

Table 3: Posterior mean and 95% credibility interval for K_1^g and k_2^g using SMM ($g = 1, 2, 3$).

Figure 3 presents the mean TAC for all the three components other than the noise component, using the posterior mean (Table 3). Superimposed are the true mean TAC for each group, and the averaged TAC from the noisy reconstructed image data. We can see that for group $g = 3$, the estimated mean is very close to both the true and the observational mean curves. But a close match is found between the estimated and observational mean TAC.

Figure 4 shows distribution of K_1 and k_2 bias and standard deviation of bias for both SMM and SCF. When we discuss bias here, we take their absolute values for discussion. In terms of K_1 for SMM, it is clear that the majority of voxels have near-zero biases, with only a few voxels having larger biases ranging from 60% to 100%. For SCF, the bias is much more spread out, with most voxels having substantially non-zero bias values spread between 0 to 73.5%. While there are fewer very large biases compared with the

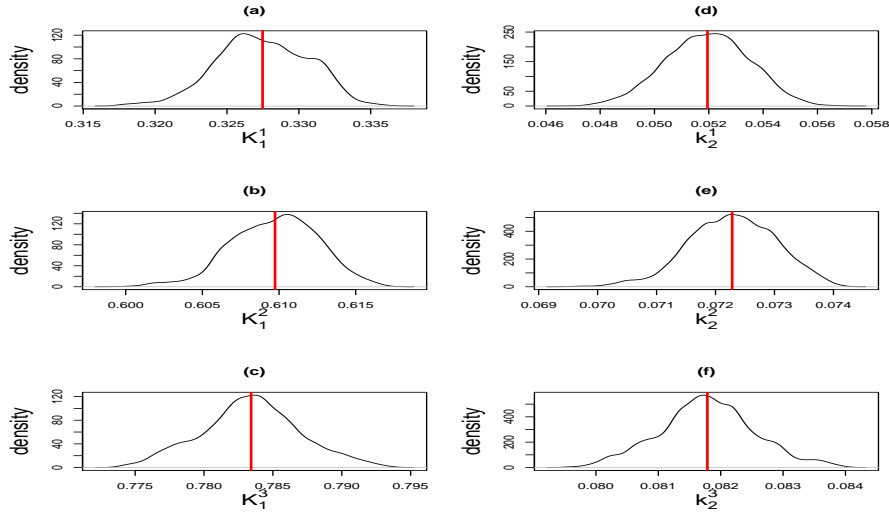
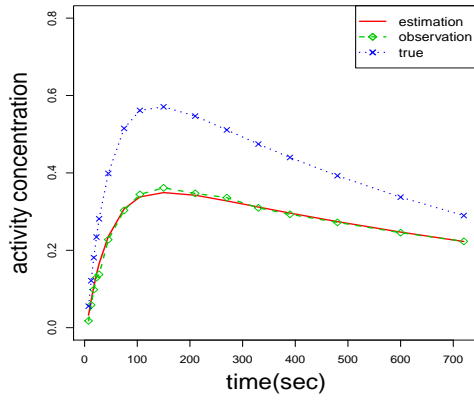


Figure 2: Posterior densities of the estimated K_1^g and k_2^g for $g = 1, 2, 3$. Red vertical lines indicate the location of the posterior means.

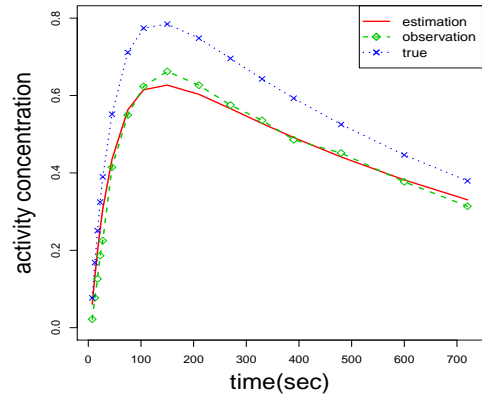
SMM			SCF			Kmeans		
96.83	3.17	0.00	73.49	26.51	0	90.42	9.58	0.00
0.35	99.3	0.35	0	100	0	0.00	98.94	1.06
0.08	2.52	97.41	2.2	18.83	78.96	0.03	2.44	97.54

Table 4: Misclassification rate matrices. For each panel, row $i = 1$ corresponds to normal tissues, row $i = 2$ corresponds to defect tissues and row $i = 3$ corresponds to noise. The diagonal entries of the matrix denote the percentage of correct classification, and the off diagonals denote misclassification, where the ij th entry denotes the percentage of observations which are classified as component j , while actually belongs to component i .

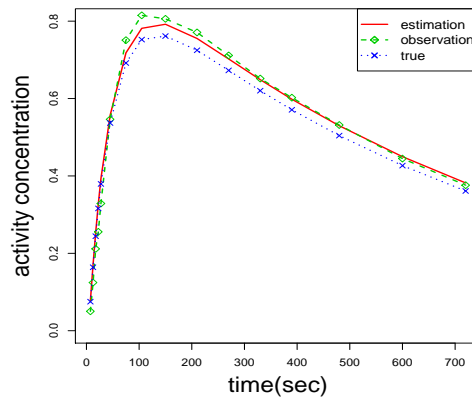
SMM. However, 85.05% of the biases are larger than SMM. From upper left figure in Figure 4, all standard deviation in SMM are allocated in 0 to 2%, while SCF totally spreads. Compared with SCF's average 5.07%, SMM has a much smaller average at 0.25%. Briefly speaking, k_2 has a similar pattern with K_1 . For SMM, it is clear that the majority of voxels have biases near zero, with only a small proportion having larger bias near 20%. For SCF, bias spreads from 0 to 194.94%, with its average as 9.66% which is two times larger than SMM's average 4.39%. For SMM, its standard deviation is no more than 5%, while SCF ranges from 0 to 118.75%. Average standard deviation of SCF is 11.88%, which is much larger than average of SMM at 0.537%. Figure 5 compares the bias and standard deviation of bias between SMM and SCF for a single slice. In order to compare SMM with SCF, we have to rescale values in some image maps. We take subfigure 5a for example. Standard deviation ranges from 0 to 40.3% and 0 to 1.3% for SCF and SMM, respectively. So we rescale them to range from 0 to 5%, which is shown in figure. Table 4 shows the misclassification matrix for SMM, SCF and Kmeans.



(a) $g = 1$



(b) $g = 2$



(c) $g = 3$

Figure 3: True, reconstructed, and estimated mean TAC curves. Plots (a) $g = 1$, (b) $g = 2$, (c) $g = 3$. Superimposed on each curve is the mean of the true TAC curve (\times) and the sample mean of the TAC using noisy data (\diamond).

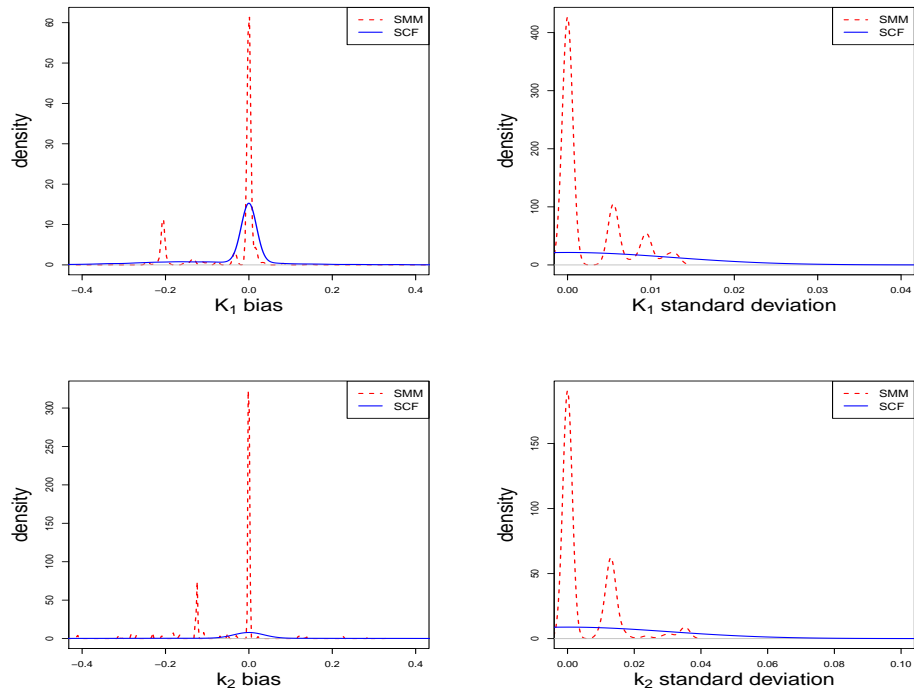


Figure 4: Distribution of the estimation bias and standard deviation of bias. Where SCF denotes standard curve fitting method (solid line), and SMM denotes spatial mixture model (dotted line).

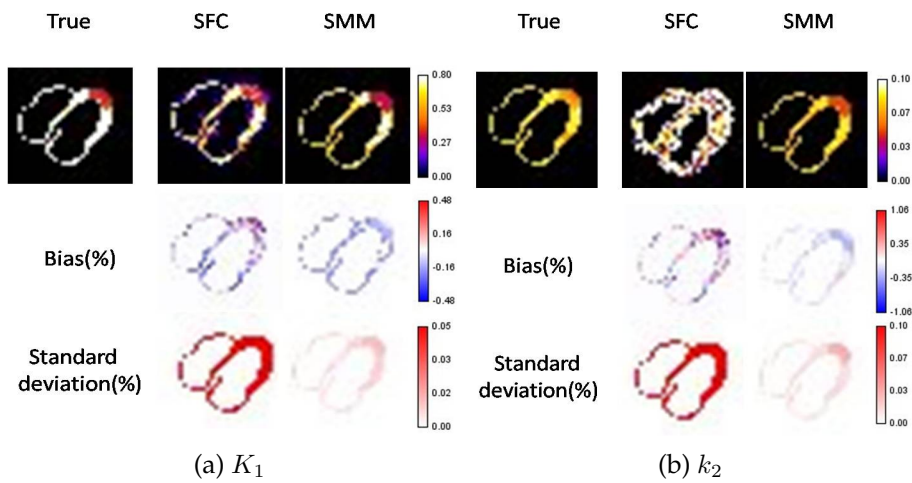


Figure 5: Parameter estimation, bias and standard deviation . Subfigure (a) presents results for K_1 , and subfigure (b) presents results for k_2 .

4 Discussions

This paper proposes a novel method, SMM, that clusters voxel-wise TACs and estimates kinetic parameters simultaneously. SMM representation allows for a flexible assumption on the distribution of the errors. Additionally, we do not assume independence between voxels, this allows us to borrow information from spatially nearby voxels. We allow the data to decide how many mixture components should be included in the model for the best fit. This was done easily via the BIC model selection criterion. An efficient MCMC algorithm in SMM allows us to provide parameter estimates, as well as uncertainty quantification simultaneously.

Table 2 lists the BIC scores obtained under SMM with different numbers of components. $G = 4$ is the optimal number selected by BIC. Each of the identified clusters aggregates statistically similar TACs. The estimated kinetic parameters can be interpreted separately for each cluster as shown in Table 3 and Figure 2. For example, the first entry in Table 3 shows that the voxels from the first cluster has a K_1 estimate of 0.3275, but the associate uncertainty of this estimate is given by the posterior distributions shown in Figure 2. If we take the corresponding 2.5 and 97.5 percentile values from the posterior samples, we can say with 95% certainly, that the true K_1 values lie between 0.3212 and 0.3331.

Figure 3 allows us to assess visually the goodness of fit of our estimation. Here the observational mean of each cluster is calculated to compare with the estimated TAC using SMM. The figures show a good agreement for all clusters. However, for $g = 1$ and $g = 2$, there's some deviation from the true TACs, this can be mainly attributed to partial volume effect (PVE). The adherence to mean of the reconstructed data shows that our model gives very good fit. However, some differences can still be seen between the estimated curve and the observational curve, most notably around the peak region in the graph $g = 2$. This suggests that there might be some mis-specification of the model we fitted.

Figure 4 shows that SMM yields smaller biases for K_1 and k_2 for the vast majority of the voxels than SCF, this is represented by the single large peak centered around 0 in the K_1 and k_2 bias graphs. However, there's a small number of voxels having bigger bias values on both K_1 and k_2 for SMM as compared with SCF, most notably the single smaller peak in the bias graph. This maybe due to the fact that there possibly should have been another cluster centered at the very high values of K_1 , but the algorithm fails to detect it, due to the very small number of such voxels and the noise level present in the data. Applying a denoising step prior to the analysis could be useful towards detecting larger numbers of clusters. The standard deviation of bias sees an improvement (reduce average from 11% to 0.5%) over SCF, suggesting a robustness in the parameter estimation approach suggested here. The difference between SMM and SCF for bias and standard deviations of bias is clearly illustrated in Figure 5.

Looking at the diagonal entries of the misclassification matrices (Table 4), SMM performs the best out of all the methods. The model correctly classifies the defect tissues with 99.3% accuracy (282 out of 284 voxels), while SCF obtains a 100% correct classification for the defect tissues. But its false-positive rate for the defect tissues is about 45.32%, whereas this number is about 5.69% for SMM and 12.02% for the Kmeans method. The classification results are similar between SMM and Kmeans, although SMM presents a 51% reduction in misclassification rate when compared directly with Kmeans.

It takes about 31 hours to complete all 6000 iterations for each noise-realization. We use the first 3000 iterations as burn-in. As we look at trace plot of parameters, we found that all the parameters converge quite quickly. In practice, 4000 iterations are sufficient

for inference. Parallel MCMC can be adopted to save time. Four Markov chains can be implemented simultaneously ending with 2000 iterations. For each Markov chain, 1000 iterations are considered as burn-in. Therefore, there are 4000 iterations in total. As a result, the total running time will be reduced to 10 hours approximately. Parallel computation or other inference methods, say, variational bayes (Attias 2000) can be adopted to speed up this process as well.

In the future, three directions are considered to develop our approach further. First, we can relax the within cluster homogeneity assumption, this is easily achievable by relaxing the mean of the normal mixture to allow them to vary for each voxel observation. However this substantially increases the number of parameter that needs to be estimated and presents a computational challenge. Second, we can see from Figure 3 that there seems exist systematic error in data. Even we have fitted our data very well, there is nonignorable difference between estimation TAC and true TAC. This is caused by reconstruction step. Therefore, we plan to use sinogram data rather than reconstructed data to estimate kinetic parameters. Third, SMM can be applied to two-compartment kinetic model without too much modification. While SCF will encounter some issues. For its nonlinear term in kinetic model, it is problematic to choose proper basis functions.

Our approach is not limited to dynamic PET. It can also be applied to dynamic imaging in other imaging modalities, such as dynamic Single Photon Emission Tomography (SPECT), dynamic contrast enhanced CT (DCE-CT), and dynamic contrast enhanced MR (DCE-MR).

5 Conclusion

This paper proposes a novel approach, SMM, to infer parametric PET image. SMM can be used to estimate kinetic parameters and classify voxels with similar kinetic parameters simultaneously. We adopt MRF to incorporate the spatial dependence of voxels. We developed an efficient MCMC algorithm for the computation, which simultaneously computes all unknown parameters, including the spatial smoothness parameter β in the Potts model. The method provides parameter uncertainty estimation. We used simulated data to evaluate the performance of SMM as compared with SCF. SMM yields much smaller bias and variance on kinetic parameters than SCF. Therefore, SMM fits data better and is more robust than SCF. Given its flexibility, SMM can be easily extended to more advanced kinetic models, such as the two-compartment tissue model.

Acknowledgements

This research was supported in part by UNSW 2014 Science Silver Star grant and NIH grants R01-HL118261 and R01-HL110241.

Appendix

Markov chain Monte Carlo

We use MCMC for sampling from posterior distribution, which is a product of the likelihood function given in Equation 2.4 and the priors as defined in Section 2.3.2, denoted as $f(K_1^1), f(K_1^2), \dots, f(K_1^{G-1}), f(k_2^1), f(k_2^2), \dots, f(k_2^{G-1}), f(\mu_{g^*}^1), \dots, f(\mu_{g^*}^T), f(\sigma^{2,1}), \dots, f(\sigma^{2,T}), f(\beta)$. The first term on the right side of Equation 2.4 is given by

$$f(y_i|z_i = g, \boldsymbol{\mu}_g, \boldsymbol{\Sigma}) = (2\pi)^{-T/2} |\boldsymbol{\Sigma}|^{-1/2} \exp\left(-\frac{1}{2}(y_i - \boldsymbol{\mu}_g)' \boldsymbol{\Sigma}^{-1} (y_i - \boldsymbol{\mu}_g)\right)$$

The second term on the right side of the equation is given by

$$f(\mathbf{z}|\beta) = \frac{1}{C(\beta)} \exp\left\{\beta \sum_{i \sim j} I(z_i = z_j)\right\}$$

which is based on the Potts model. The partition function $C(\beta)$ is estimated offline using thermal dynamic integration (Green and Richardson (2002)). We use a 8 nearest neighbour structure over our ROI to define the neighbourhood for the Potts model.

Our computational algorithm proceeds as follows: .

Step 1 Set $l = 1$ and initialise parameters $K_1^{1,(0)}, k_2^{1,(0)}, \dots, K_1^{G-1,(0)}, k_2^{G-1,(0)}, \boldsymbol{\mu}_{g^*}^{(0)}, \sigma^{2,1,(0)}, \dots, \sigma^{2,T,(0)}, \mathbf{z}^{(0)}, \beta^{(0)}$.

Step 2 Update K_1^g , for $g = 1, \dots, G - 1$. Simulate a new value

$$K_1^{g'} \sim N(K_1^{g,(l-1)}, \delta_{K_1}^2)$$

and compute $\boldsymbol{\mu}'_g$ with $K_1^{g'}$, according to Equation (2.3). Set $K_1^{g,(l)}$ to $K_1^{g'}$ with probability α , where

$$\alpha = \min \left\{ 1, \frac{\prod_{i \in \{i: z_i^{(l-1)} = g\}} f(y_i | z_i^{(l-1)}, \boldsymbol{\mu}'_g, \boldsymbol{\Sigma}^{(l-1)}) f(K_1^{g'})}{\prod_{i \in \{i: z_i^{(l-1)} = g\}} f(y_i | z_i^{(l-1)}, \boldsymbol{\mu}_g^{(l-1)}, \boldsymbol{\Sigma}^{(l-1)}) f(K_1^{g,(l-1)})} \right\}.$$

Otherwise, set $K_1^{g,(l)}$ to $K_1^{g,(l-1)}$.

Step 3 Update k_2^g , For $g = 1, \dots, G - 1$. Analogously to Step 2.

Step 4 Update $\mu_{g^*}^t$, for $t = 1, \dots, T$. Simulate a new value

$$\mu_{g^*}^{t'} \sim N(\mu_{g^*}^{t,(l-1)}, \delta_{\mu_{g^*}}^2).$$

Set $\mu_{g^*}^{t,(l)}$ to $\mu_{g^*}^{t'}$ with probability α , where

$$\alpha = \min \left\{ 1, \frac{\prod_{i \in \{i: z_i^{(l-1)} = g^*\}} f(y_i | z_i^{(l-1)}, \mu_{g^*}^{t'}, \boldsymbol{\Sigma}^{(l-1)}) f(\mu_{g^*}^{t'})}{\prod_{i \in \{i: z_i^{(l-1)} = g^*\}} f(y_i | z_i^{(l-1)}, \mu_{g^*}^{t,(l-1)}, \boldsymbol{\Sigma}^{(l-1)}) f(\mu_{g^*}^{t,(l-1)})} \right\}.$$

Otherwise, set $\mu_{g^*}^{t,(l)}$ to $\mu_{g^*}^{t,(l-1)}$.

Step 5 Update $\sigma^{2,t}$, for $t = 1, \dots, T$. Simulate from the Inverse Gamma distribution

$$\sigma^{2,t,(l)} \sim IG \left(n/2 + a, \frac{1}{2} \sum_{i=1}^n (y_i^t - \boldsymbol{\mu}_g^{t,(l)})^2 + b \right).$$

Step 6 Update \mathbf{z} . Each $i = 1, \dots, N$, compute

$$w_g = MVN(y_i; f(K_1^g, k_2^g), \boldsymbol{\Sigma}) + \exp\{\beta^{(l-1)} \sum_{j,j \in \partial i} I(z_j^{(l-1)} = g)\}, \quad g = 1, \dots, G,$$

and normalise $w'_g = w_g / \sum_{g=1}^G w_g$, where $f(K_1^g, k_2^g)$ denotes Equation 2.3. ∂i denotes the set of neighbours of vertex i , and $I(\cdot)$ denotes indicator function taking value 1 if $z_j^{(l-1)} = g$ and 0 otherwise. Set $z_i^{(l)}$ according to the Multinomial distribution

$$z_i^{(l)} \sim MN(w'_1, \dots, w'_G).$$

Step 7 Update β . Simulate a new value

$$\beta' \sim N(\beta^{(l-1)}, \delta_\beta^2)$$

and set $\beta^{(l)}$ to β' with probability α , where

$$\alpha = \min \left\{ 1, \frac{f(\mathbf{z}^{(l)} | \beta') f(\beta')}{f(\mathbf{z}^{(l)} | \beta^{(l-1)}) f(\beta^{(l-1)})} \right\}.$$

Otherwise, set $\beta^{(l)}$ to $\beta^{(l-1)}$. $f(\mathbf{z} | \beta)$.

Step 8 set $l = l + 1$, if $l < L$, go to Step 2.

References

- Aristophanous, M., B. C. Penney, M. K. Martel, and C. A. Pelizzari (2007). A Gaussian mixture model for definition of lung tumor volumes in positron emission tomography. *Medical Physics* 34(11), 4223.
- Ashburner, J., J. Haslam, C. Taylor, V. J. Cunningham, and T. Jones (1996). *Quantification of Brain Function Using PET*, Chapter A cluster analysis approach for the characterization of dynamic PET data, pp. 301–306. Academic Press.
- Attias, H. (2000). A variational Bayesian framework for graphical models. *Advances in neural information processing systems* 12(1-2), 209–215.
- Cerqueira, M. D., N. J. Weissman, V. Dilsizian, A. K. Jacobs, S. Kaul, W. K. Laskey, and et al. (2002). Standardized Myocardial segmentation and nomenclature for tomographic imaging of the heart: A statement for healthcare professionals from the Cardiac Imaging Committee of the Council on Clinical Cardiology of the American Heart Association. *J Nucl Cardiol* 9, 240–245.
- Chen, J. L., S. R. Gunn, M. S. Nixon, and R. N. Gunn (2001). *Information Processing in Medical Imaging*, Volume 2082 of *Lecture Notes in Computer Science*, Chapter Markov Random Field models for segmentation of PET images, pp. 468–474. Springer Berlin Heidelberg.
- Fernández, C. and P. J. Green (2002). Modelling spatially correlated data via mixtures: a bayesian approach. *Journal of the royal statistical society: series B (Statistical methodology)* 64(4), 805–826.
- Foster, B., U. Bagci, A. Mansoor, Z. Xu, and D. J. Mollura (2014). A review on segmentation of positron emission tomography. *Computers in Biology and Medicine* 50, 76–96.
- Frühwirth-Schnatter, S. (2011). *Mixtures: Estimation and Applications*, Chapter Dealing with label switching under model uncertainty. Wiley.
- Green, P. J. and S. Richardson (2002). Hidden Markov Models and disease mapping. *Journal of the American statistical association* 97(460), 1055–1070.
- Gunn, R. N., S. R. Gunn, F. E. Turkheimer, J. A. Aston, and V. J. Cunningham (2002). Positron Emission Tomography compartmental models; a basis pursuit strategy for kinetic modeling. *Journal of Cerebral Blood Flow & Metabolism* 22(12), 1425–1439.
- Gunn, R. N., A. A. Lammertsma, S. P. Hume, and V. J. Cunningham (1997). Parametric imaging of ligand-receptor binding in PET using a simplified reference region model. *Neuroimage* 6(4), 279–287.
- Guo, H., R. Renaut, K. Chen, and E. Reiman (2003). Clustering huge data sets for parametric PET imaging. *BioSystems* 71, 81–92.
- Hatt, M., C. Cheze le Rest, A. Turzo, C. Roux, and D. Visvikis (2009). A fuzzy locally adaptive Bayesian segmentation approach for volume determination in PET. *IEEE Trans Med Imaging* 28(6), 881–93.
- Huang, S.-C. and Y. Zhou (1998). Spatially-coordinated regression for image-wise model fitting to dynamic PET data for generating parametric images. *Nuclear Science, IEEE Transactions on* 45(3), 1194–1199.
- Hudson, H. M. and R. S. Larkin (1994). Accelerated image reconstruction using ordered subsets of projection data. *Medical Imaging, IEEE Transactions on* 13(4), 601–609.

- Kamasak, M. E., C. A. Bouman, E. D. Morris, and K. Sauer (2005). Direct reconstruction of kinetic parameter images from dynamic pet data. *Medical Imaging, IEEE Transactions on* 24(5), 636–650.
- Kim, J., W. Cai, D. Feng, and S. Eberl (2006). Segmentation of VOI from multidimensional dynamic PET images by intergrating spatial and temporal features. *IEEE Transactions on information technology in biomedicine* 10, 637–646.
- Lammertsma, A. A. and S. P. Hume (1996). Simplified reference tissue model for PET receptor studies. *Neuroimage* 4(3), 153–158.
- Lin, Y., J. Haldar, Q. Li, P. Conti, and R. Leahy (2014). Sparsity constrained mixture modeling for the estimation of kinetic parameters in dynamic PET. *IEEE Trans Med Imaging* 33(173-185).
- Mohy-ud Din, H., N. A. Karakatsanis, M. A. Lodge, J. Tang, and A. Rahmim (2014). Parametric myocardial perfusion pet imaging using physiological clustering. In *SPIE Medical Imaging*, pp. 90380P–90380P. International Society for Optics and Photonics.
- Morris, E. D., C. J. Endres, K. C. Schmidt, B. T. Christian, R. F. Muzic Jr., and R. E. Fisher (2004). *Emission Tomography*, Chapter Kinetic modelling in positron emission tomography, pp. 499–540. Elsevier.
- Nye, J. A., J. R. Votaw, N. Jarkas, D. Purselle, V. Camp, J. D. Bremner, C. D. Kilts, C. B. Nemeroff, and M. M. Goodman (2008). Compartmental modeling of 11c-homadam binding to the serotonin transporter in the healthy human brain. *Journal of Nuclear Medicine* 49(12), 2018–2025.
- O’Sullivan, F. and A. Saha (1999). Use of ridge regression for improved estimation of kinetic constants from PET data. *Medical Imaging, IEEE Transactions on* 18(2), 115–125.
- Saad, A., B. Smith, G. Hamarneh, and T. Möller (2007). Simultaneous segmentation, kinetic parameter estimation, and uncertainty visualization of dynamic PET images. In *Medical Image Computing and Computer-Assisted Intervention–MICCAI 2007*, pp. 726–733. Springer.
- Schwarz, G. et al. (1978). Estimating the dimension of a model. *The Annals of Statistics* 6(2), 461–464.
- Segars, W. (2000). *Development of a new dynamic NURBS-based cardiac torso (NCAT) phantom*. Ph. D. thesis, University of North Carolina.
- Slifstein, M., B. Kolachana, E. Simpson, P. Tabares, B. Cheng, M. Duvall, W. G. Frankle, D. Weinberger, M. Laruelle, and A. Abi-Dargham (2008). COMT genotype predicts cortical-limbic D1 receptor availability measured with 11C; NNC112 and PET. *Molecular psychiatry* 13(8), 821–827.
- Steele, R. J. and A. E. Raftery (2009). Performance of Bayesian model selection criteria for Gaussian mixture models. *Dept. Stat., Univ. Washington, Washington, DC, Tech. Rep* 559.
- Velamuru, P. K., R. A. Renaut, H. Guo, and K. Chen (2005). Robust clustering of positron emission tomography data. In *In Joint Conference of the Classification Society of North America and INterface Foundation of North America*.
- Wang, G. and J. Qi (2009). Generalized algorithms for direct reconstruction of parametric images from dynamic PET data. *IEEE Trans Med Imaging* 28, 1717–26.

Wu, F.-Y. (1982). The Potts model. *Reviews of modern physics* 54(1), 235.

Zhou, Y., J. A. Aston, and A. M. Johansen (2013). Bayesian model comparison for compartmental models with applications in positron emission tomography. *Journal of Applied Statistics* 40(5), 993–1016.